

# Vector Boson Fusion versus Gluon Fusion

Chen-Hsun Chan<sup>1</sup>, Kingman Cheung<sup>1,2,3</sup>, Yi-Lun Chung<sup>1</sup>, and Pai-Hsien Hsu<sup>1</sup>

<sup>1</sup> *Department of Physics,*

*National Tsing Hua University,*

*Hsinchu 300, Taiwan*

<sup>2</sup> *Physics Division, National Center for Theoretical Sciences, Hsinchu, Taiwan*

<sup>3</sup> *Division of Quantum Phases and Devices,*

*School of Physics, Konkuk University,*

*Seoul 143-701, Republic of Korea*

(Dated: March 12, 2022)

## Abstract

Vector-boson fusion (VBF) is a clean probe of the electroweak-symmetry breaking (EWSB), which inevitably suffers from some level of contamination due to the gluon fusion (ggF). In addition to the jet variables used in the current experimental analysis, we analyze a few more jet-shape variables defined by the girth and integrated jet-shape. Taking  $H \rightarrow WW^* \rightarrow e\nu\mu\nu$  and  $H \rightarrow \gamma\gamma$  as examples, we perform the analysis with a new technique of 2-step boosted-decision-tree method, which significantly reduces the contamination of the ggF in the VBF sample, thus, providing a clean environment in probing the EWSB sector.

## I. INTRODUCTION

The origin of mass is one of the most fundamental questions for our existence. Particle physics explains the origin of mass by the electroweak symmetry breaking (EWSB). Before the electroweak symmetry is broken the whole Universe is filled up with a Higgs field and every particle is massless. When this Higgs field develops a vacuum expectation value (VEV), a particular direction in the field space is chosen and the symmetry is broken. Particles then acquire masses proportional to the VEV of the Higgs field.

The discovery of the Higgs boson at the Large Hadron Collider (LHC) in 2012 [1] was a remarkable evidence of the EWSB and its properties help us to fully understand the nature of the EWSB. The long-sought standard model (SM) Higgs boson was proposed more than 50 years ago, which breaks the electroweak symmetry in order to give masses to gauge bosons and fermions. If the discovered boson is really the SM Higgs boson or something similar, the investigation of its properties would give a lot of information about the EWSB.

The measurements of the properties of the Higgs boson, including mass, total width, production cross sections, and branching ratios will give us a lot of information on its gauge and Yukawa couplings, thus indirectly the details inside the EWSB sector, which could be as complicated as one can imagine. The current dominant production mechanism of the Higgs boson is the gluon fusion (ggF), followed by a small fraction by vector-boson fusion (VBF). Although the ggF could provide useful information on the top-Yukawa coupling, the VBF is the ultimate testing ground for probing the EWSB section, because the longitudinal component of the  $W$  and  $Z$  bosons originate from the EWSB sector itself.

The approach of isolating the VBF from ggF relies on the properties of the jets involved in the process and a few techniques were developed two decades ago, namely, forward-jet tagging [2] and central-jet vetoing [3]. The two accompanying jets carry most of the jet energy of the incoming quark partons, and thus they are very energetic and very forward. One can also make use of the wide rapidity gap between those two jets [4]. On the other hand, the jets involved in the ggF come directly from the QCD radiation. Naively, we would expect a very rich event sample of VBF from the experimental data with all the sophisticated jet selection cuts. Nevertheless, with much improved accuracy in the N<sup>3</sup>LO calculation of ggF [5] the level of ggF in such selection is indeed not negligible but a substantial fraction of the VBF+ggF sample. We shall use the word “contamination” of the VBF sample to

denote the fraction of ggF in the VBF+ggF sample.<sup>1</sup> Thus, the “contamination” of the VBF sample due to ggF is defined by

$$\frac{\text{ggF}}{\text{VBF} + \text{ggF}}.$$

It stands at a level about 25% in the current experimental studies [6, 7]. The purer the VBF sample, the better one can probe the EWSB sector. The current experimental status of discriminating the VBF from ggF was based on a set of jet kinematical variables ( $M_{jj}$ ,  $\Delta\eta_{jj}$ , ...), a set of jet-shape variables, and those kinematic variables depending on the decay channel of the Higgs boson. A standard boosted-decision-tree (BDT) approach was employed to achieve the current purity of the VBF sample and to reduce the contamination of the ggF. Note that the purity of the VBF is defined here as

$$\frac{\text{VBF}}{\text{VBF} + \text{ggF} + \text{other SM background}}.$$

In this study, we employ a 2-step BDT analysis to further reduce the contamination by ggF, thus a purer VBF sample is achieved without significant loss in event rates. This is the main result of this work. We illustrate our analysis for the decay channels of  $H \rightarrow WW^* \rightarrow e\nu\mu\nu$  and  $H \rightarrow \gamma\gamma$ .

The organization is as follows. In the next section, we describe the Monte-Carlo simulations, and in Sec. III procedures in the BDT analysis. We present the results in Sec. IV and conclude in Sec. V.

## II. EVENT SAMPLES PREPARATION

In order to compare directly with the current status on purity of VBF samples of ATLAS [6, 7], we follow their preparation of event samples as closely as possible. We simulate the event samples for Higgs boson production including those via VBF and ggF using the PowHEG [8–10] generator at next-to-leading-order (NLO), with input parton distribution functions (PDFs) CT10 [11], and the mass and width of the Higgs taken at  $m_H = 125\text{GeV}$  and  $\Gamma_H = 4.07\text{MeV}$ . The Higgs boson samples are normalized to the cross sections given in the ATLAS analysis for 13 TeV. Note that for  $H \rightarrow \gamma\gamma$  a parton-level cut  $105 \leq m_{\gamma\gamma} \leq 160\text{ GeV}$  (Higgs window) is applied.

<sup>1</sup> In this study, although we generate the VBF Monte-Carlo sample and ggF sample separately, we shall keep using “contamination” to denote the fraction of ggF in the sum VBF+ggF events.

All Higgs boson events are then showered and decayed into either  $WW + \text{jets}$  or  $\gamma\gamma + \text{jets}$  by PYTHIA 8 [12] and passed to DELPHES [13]<sup>2</sup> for detector-level simulation. Note that for the channel  $H \rightarrow WW^*$  each of the  $W$  bosons further decays into a charged lepton and a neutrino. Note that the charged-lepton flavors from the  $W$  boson pair are required to be different, i.e,  $e^+\mu^-$  or  $e^-\mu^+$ . Table I summarizes the event generators and the cross sections for each process.

Process	MC generator	$\sigma \cdot \mathcal{B}$ (pb)	Number of Events
VBF	POWHEG +PYTHIA 8	0.0232	553240
ggF	POWHEG +PYTHIA 8	0.297	1936340
$t\bar{t}$	MADGRAPH5_AMC@NLO +PYTHIA 8	22.6	3319440
$WW$	POWHEG +PYTHIA 8	3.10	3319440

TABLE I. Monte Carlo generators, cross sections and the generated number of events (non-normalized) used to model each signal and background process in  $WW$  decay channel at  $\sqrt{s} = 13\text{TeV}$

In the  $WW$  decay channel, we consider two main backgrounds: the SM  $t\bar{t}$  and  $WW$  production. The  $t\bar{t}$  events are generated at NLO using the MADGRAPH5\_AMC@NLO (version 2.4.3) [14], while the  $WW$  events are generated with POWHEG at NLO [15]. After then, the  $t\bar{t}$  and  $WW$  events are showered and each top quark decays into  $b + W$  with PYTHIA 8 [12]. The  $W$  bosons further decay into  $\ell + \nu$ , and the flavors of two charged leptons in each event are required to be different. Events are then passed into DELPHES for detector simulations. The event generators, cross sections, and the generated number of events for these backgrounds are also tabulated in Table I.

In the diphoton channel, we only consider one source of background:  $\gamma\gamma + jj$ , which are generated at leading-order (LO) using the MADGRAPH5\_AMC@NLO[14]. Each of the jet in  $\gamma\gamma + jj$  events is then showered into multi-jets with PYTHIA 6 [16]. Finally, events are passed into DELPHES for detector simulations. The event generators, cross sections, and the generated number of events for the backgrounds in the diphoton decay channel are also listed in Table II.<sup>3</sup>

<sup>2</sup> Version 3 is used here with the anti- $k_T$  jet algorithm using  $\Delta R = 0.4$  and  $p_{T_j}^{\min} = 20$  GeV and the

$b$ -tagging efficiency is given by  $0.80 \tanh(0.003 p_T) \frac{30}{1+0.086 p_T}$ , where  $p_T$  is given in GeV.

<sup>3</sup> The background events of  $jj\gamma\gamma$  are generated with a set of basic cuts:  $p_{T_\gamma} > 20$  GeV,  $|\eta_\gamma| < 2.5$ ,  $p_{T_j} > 20$  GeV, and  $|\eta_j| < 5$  in the generator level to avoid the divergence.

Process	Generator	$\sigma \cdot \mathcal{B}$ (pb)	Number of Events
VBF	POWHEG +PYTHIA 8	0.862	200000
ggF	POWHEG +PYTHIA 8	11.1	800000
$\gamma\gamma+jj$	MADGRAPH5_AMC@NLO +PYTHIA 6	4.12	2000000

TABLE II. Monte Carlo generators, cross sections, and the generated number of events (non-normalized) used to model each signal and background process in diphoton decay channel at  $\sqrt{s} = 13 TeV$

### III. METHODS IN BOOSTED DECISION TREES (BDT)

The dedicated event samples will undergo a series of analysis tools or methods, including preselection cuts and boosted decision tree (BDT) [17], in order to enhance the purity of the VBF among the Higgs signals and backgrounds. In general, each signal and background event has to first pass a set of kinematic preselection cuts, and then is further selected according to the BDT output. In each decay channel, we present four different methods of BDT, including the standard BDT, which mainly follows the method in ATLAS so that we can make directly comparison to the other three new methods of BDT. Tables IV and V summarize the procedures for  $H \rightarrow WW^*$  and  $H \rightarrow \gamma\gamma$ , respectively. The details are described in the following two subsections.

We used the Gradient BDT with the BDT parameters given in Table III. We have varied a few slightly different settings, but the outputs do not have significant changes. The BDT is trained after the preselection cuts to improve the statistics of simulated samples used in the training. The variables can be ranked by their *rankings* in the training. The BDT output score is defined in the

Parameter	value
NTrees (Number of trees in the forest)	1000
Shrinkage	0.1
nCuts (number of steps during node cut optimization)	20
MaxDepth (Max depth of the decision tree allowed)	2

TABLE III. The BDT parameters that are used in various BDT runs, except for the 11-variable BDT and the step-2 BDT used in  $H \rightarrow WW^*$  channel that used NTrees = 800 to avoid over-training. The event rates stay the same with the change in NTrees.

range of  $-1$  to  $1$ , with signal-like events having a score close to  $1$  and background-like events a score close to  $-1$ .

### A. $H \rightarrow WW^* \rightarrow e\nu\mu\nu$

The event samples for the VBF  $H \rightarrow WW^*$  signal, ggF, and the SM backgrounds have to pass the preselection cuts which were given in the current ATLAS analysis for the SM Higgs boson decaying into  $WW^*$  in the different lepton-flavor category, which are described as follows:

1.  $N_j \geq 2$ ;
2.  $p_T^j > 25 \text{ GeV}$  ( $|\eta^j| < 2.4$ ) and  $p_T^j > 30 \text{ GeV}$  ( $2.4 < |\eta^j| < 4.4$ );
3.  $p_T^{\ell 1} > 25 \text{ GeV}$  and  $p_T^{\ell 2} > 15 \text{ GeV}$ ;
4.  $m_{\ell\ell} > 10 \text{ GeV}$ , where  $m_{\ell\ell}$  is the invariant mass of two leading leptons;
5.  $N_b = 0$ ;
6. Outside-lepton veto (OLV), and central-jet veto (CJV) [6]

**Standard BDT** Following the current procedures of the ATLAS analysis, the signal sample of VBF and the background samples of simulated ggF, simulated  $t\bar{t}$ , and simulated  $WW$  events are used to train the BDT. We call this one the standard BDT, with which we shall compare. The following 8 variables are fed into the BDT:

1.  $m_{jj}$ : invariant mass of two leading jets;
2.  $\Delta\eta_{jj} \equiv |\eta_{j1} - \eta_{j2}|$ ;
3.  $p_T^{\text{sum}} \equiv p_T^{\ell\ell} + p_T^{\text{miss}} + \sum p_T^j$ ;
4.  $\sum m_{\ell_j} \equiv m_{\ell_1, j_1} + m_{\ell_1, j_2} + m_{\ell_2, j_1} + m_{\ell_2, j_2}$ ;
5.  $\sum C_\ell \equiv \sum \left| \eta_\ell - \frac{\sum \eta_{jj}}{2} \right| / \frac{\Delta\eta_{jj}}{2}$ ;
6.  $m_{\ell\ell}$ ;
7.  $\Delta\phi_{\ell\ell}$ ;

Objective	Standard BDT	11-Var BDT	7-Var BDT	2-step BDT
Preselection		$N_j \geq 2, N_b = 0,$ $p_T^j > 25 \text{ GeV } ( \eta^j  < 2.4) \text{ \& } p_T^j > 30 \text{ GeV } (2.4 <  \eta^j  < 4.4),$ $p_T^{\ell 1} > 25 \text{ GeV}, p_T^{\ell 2} > 15 \text{ GeV},$ $m_{\ell\ell} > 10 \text{ GeV},$ OLV, CJV		
1 <sup>st</sup> step				
Signal sample	VBF	VBF	VBF	VBF
Bkg. sample	ggF & $t\bar{t}$ & $WW$	ggF & $t\bar{t}$ & $WW$	ggF & $t\bar{t}$ & $WW$	$t\bar{t}$ & $WW$
BDT inputs	$m_{jj}, \Delta\eta_{jj}, p_T^{\text{sum}},$ $\sum m_{\ell j}, \sum C_\ell,$ $m_{\ell\ell}, \Delta\phi_{\ell\ell}, m_T$	$m_{jj}, \Delta\eta_{jj}, p_T^{\text{sum}},$ $\sum m_{\ell j}, \sum C_\ell,$ $m_{\ell\ell}, \Delta\phi_{\ell\ell}, m_T$	$m_{jj}, \Delta\eta_{jj},$ $p_T^{\text{sum}}, \sum m_{\ell j},$ $\sum g_j, \Psi_c, \Psi_s$	$m_{jj}, \Delta\eta_{jj}, p_T^{\text{sum}},$ $\sum m_{\ell j}, \sum C_\ell,$ $m_{\ell\ell}, \Delta\phi_{\ell\ell}, m_T$
2 <sup>nd</sup> step				
Signal sample	-	-	-	VBF
Bkg. sample	-	-	-	ggF
BDT inputs	-	-	-	$m_{jj}, \Delta\eta_{jj},$ $p_T^{\text{sum}}, \sum m_{\ell j},$ $\sum g_j, \Psi_c, \Psi_s,$

TABLE IV. Summary of each analytic method for  $H \rightarrow WW^*$ 

8. transverse mass:  $m_T \equiv \sqrt{(E_T^{\ell\ell} + p_T^{\nu\nu})^2 - |\mathbf{p}_T^{\ell\ell} + \mathbf{p}_T^{\nu\nu}|^2}$ , where  $E_T^{\ell\ell} = \sqrt{(p^{\nu\nu})^2 + (m_{\nu\nu})^2}$ ,  $\mathbf{p}^{\nu\nu}(\mathbf{p}^{\ell\ell})$  is the vector sum of the neutrino (lepton) transverse momenta, and  $p^{\nu\nu}(p^{\ell\ell})$  is its modulus.

The distributions of these variables for signal and backgrounds are shown in Fig. 1, in which we can clearly see the capability of each of the variables in discriminating between the signal and backgrounds.

**11-variable BDT** The signal and background training samples are the same as the standard BDT. In addition to the 8 variables in standard BDT, 3 more jet-shape variables [18] are employed in this 11-variable BDT analysis:

1. girth summed over two leading jets:  $\sum g_j \equiv \sum_{j,i \in j} \frac{p_{T,i}^j r_i^j}{p_T^j}$
2. the central integrated jet shape:  $\Psi_c \equiv \frac{1}{N} \sum_{j=1}^2 \sum_{i \in j} \frac{p_{T,i}^j (0 < r_i^j < 0.1)}{p_T^j}$
3. the side integrated jet shape:  $\Psi_s \equiv \frac{1}{N} \sum_{j=1}^2 \sum_{i \in j} \frac{p_{T,i}^j (0.1 < r_i^j < 0.2)}{p_T^j}$

The distributions of these jet-shape variables for the signal and backgrounds are shown in Fig. 2.

**7-variable BDT** Analyzing the distributions shown in Figs. 1 and Fig. 2, we find that 7 of the variables are sufficient in distinguishing between the VBF events and the others:  $m_{jj}$ ,  $\Delta\eta_{jj}$ ,  $p_T^{\text{sum}}$ ,  $\sum m_{lj}$ ,  $\sum g_j$ ,  $\Psi_c$ , and  $\Psi_s$ . The choice of these 7 variables out of the 11 variables is based on the ranking output. Thus, in this method only these 7 variables are used in discriminating VBF from the ggF and backgrounds. The signal and background training samples are the same as the standard BDT.

**2-step BDT** This is the new approach that we adopt in this study. We separate the training of the BDT in two steps, in which the BDT is trained for VBF against the SM backgrounds and against the ggF, respectively.

- The first step: the VBF signal sample is trained against the SM background samples of  $t\bar{t}$  and  $WW$  events. In this step, the variables used are the same as the standard BDT.
- The second step: after imposing the selection cuts obtained in the first-step-BDT output  $O_{\text{BDT}}^1$ , the event samples will further undergo the second-step BDT, in which the VBF signal sample is trained against the ggF sample only. In this step, the variables used are the same as 7-Var BDT.

## B. $H \rightarrow \gamma\gamma$

Similar to the procedures in  $H \rightarrow WW^*$ , the events samples for the VBF  $H \rightarrow \gamma\gamma$  signal, ggF, and the SM background have to pass the preselection cuts, which were given in the current ATLAS analysis for the SM  $H \rightarrow \gamma\gamma$  in the VBF enriched category. The requirements are described as follows:

1.  $N_j \geq 2$ ;
2.  $p_T^j > 25 \text{ GeV}$  ( $|\eta^j| < 2.4$ ) and  $p_T^j > 30 \text{ GeV}$  ( $2.4 < |\eta^j| < 4.4$ );



3.  $\Delta\eta_{jj} > 2$ ;
4.  $105 \leq m_{\gamma\gamma} \leq 160 \text{ GeV}$ ;
5.  $p_T^{j1} \geq 0.35m_{\gamma\gamma}$  and  $p_T^{j2} \geq 0.25m_{\gamma\gamma}$ ;
6.  $|\eta^*| < 5$ , where  $|\eta^*| \equiv |\eta_{\gamma\gamma} - (\eta_{j1} + \eta_{j2})|/2$ .

Objective	Standard BDT	9-Var BDT	5-Var BDT	2-step BDT
Preselection	$N_j \geq 2,$ $p_T^j > 25 \text{ GeV } ( \eta^j  < 2.4) \text{ \& } p_T^j > 30 \text{ GeV } (2.4 <  \eta^j  < 4.4),$ $\Delta\eta_{jj} > 2,$ $105 \leq m_{\gamma\gamma} \leq 160 \text{ GeV},$ $p_T^{j1} \geq 0.35m_{\gamma\gamma} \text{ and } p_T^{j2} \geq 0.25m_{\gamma\gamma}$ $ \eta^*  < 5$			
1 <sup>st</sup> step				
Signal sample	VBF	VBF	VBF	VBF
Bkg. sample	ggF & $\gamma\gamma + jj$	ggF & $\gamma\gamma + jj$	ggF & $\gamma\gamma + jj$	$\gamma\gamma + jj$
BDT inputs	$m_{jj}, \Delta\eta_{jj}, p_{Tt},$ $\Delta R_{\gamma,j}^{\min},  \eta^* , \phi^*$	$m_{jj}, \Delta\eta_{jj}, p_{Tt},$ $\Delta R_{\gamma,j}^{\min},  \eta^* , \phi^*,$	$m_{jj}, \Delta\eta_{jj},$ $\sum g_j, \Psi_c, \Psi_s,$	$m_{jj}, \Delta\eta_{jj}, p_{Tt},$ $\Delta R_{\gamma,j}^{\min},  \eta^* , \phi^*,$ $\sum g_j, \Psi_c, \Psi_s$
2 <sup>nd</sup> step				
Signal sample	-	-	-	VBF
Bkg. sample	-	-	-	ggF
BDT inputs	-	-	-	$m_{jj}, \Delta\eta_{jj},$ $\sum g_j, \Psi_c, \Psi_s,$

TABLE V. Summary of each analytic method for  $H \rightarrow \gamma\gamma$ 

**Standard BDT** Following the current procedures in the ATLAS analysis, the signal sample of VBF and the background samples of ggF events and simulated  $\gamma\gamma + jj$  events are used to train the BDT. Again, this is the standard BDT. The following 6 variables are inputs to the BDT:

1.  $m_{jj}$ ;

2.  $\Delta\eta_{jj}$ ;
3.  $p_{Tt} \equiv |(\mathbf{p}_T^{\gamma_1} + \mathbf{p}_T^{\gamma_2}) \times \hat{t}|$ , where  $\hat{t} = (\mathbf{p}_T^{\gamma_1} - \mathbf{p}_T^{\gamma_2}) / |\mathbf{p}_T^{\gamma_1} - \mathbf{p}_T^{\gamma_2}|$ ;
4.  $\Delta R_{\gamma,j}^{\min} \equiv$  the minimum separation between the leading/subleading photon and the leading/subleading jet;
5.  $|\eta^*|$ ;
6.  $\phi^* \equiv$  the azimuthal angle between the diphoton and the dijet system.

The distributions of these variables for the signal and backgrounds are shown in Fig. 3.

**9-variable BDT** The signal and background training samples are the same as the standard BDT. In addition to the 6 variables in the standard BDT, 3 more jet-shape variables are used in this 9-variable BDT:  $\sum g_j$ ,  $\Psi_c$ ,  $\Psi_s$ , whose distributions are shown in Fig. 4.

**5-variable BDT** Analyzing the distributions of the above 9 variables we find five most powerful variables in discriminating between VBF and ggF. They are  $m_{jj}$ ,  $\Delta\eta_{jj}$ ,  $\sum g_j$ ,  $\Psi_c$ ,  $\Psi_s$ , as shown in Fig. 3 and Fig. 4.

**2-step BDT** Again, this is the new approach that we are adopting in this study. We separate the training of the BDT in two steps:

- The first step: the VBF signal sample is trained against the background sample of  $\gamma\gamma + jj$  events. In this step, the variables used are the same as the standard BDT.
- The second step: after imposing the selection cuts obtained in the first-step-BDT output  $O_{\text{BDT}}^1$ , the event samples will further undergo the second-step BDT, in which the VBF signal samples is trained against the ggF sample. In this step, the variables used are the same as 5-Var BDT.

## IV. RESULTS

### A. $H \rightarrow WW^* \rightarrow e\nu\mu\nu$

Figure 5 shows the linear correlations between any two of the variables used in the 11-Var BDT for the channel  $H \rightarrow WW^*$ . From the figure we can see very strong correlations appear among the 3 jet-shape variables, and among  $\sum m_{\ell j}$ ,  $\Delta\eta_{jj}$ , and  $m_{jj}$  in both the signal and backgrounds.

A sizeable correlation also appears between  $m_{\ell\ell}$  and  $\Delta\phi_{\ell\ell}$  in both the signal and backgrounds. In addition, in order to avoid overtraining in BDT analyses, we show the BDT output distributions for both the training and testing samples in Fig. 6.

The results of our analyses for the channel  $H \rightarrow WW^*$  are summarized in Table VI. The final numbers of the remained VBF events for all methods are all around 5.1, in order to have direct comparisons among various methods used here. Comparing between the standard BDT and the 11-Var BDT, the latter which used 3 jet-shape variables, can enhance the VBF purity and at the same time reduce the ggF contamination by about 2%. When we focus on distinguishing just between the VBF and ggF event samples, the 7-Var BDT using the most powerful 7 variables is introduced and can further decrease the ggF contamination by about 1%. However, this method sacrifices the discrimination between the VBF sample and the other SM backgrounds, and thus lowers the VBF purity to only 50.5%.

To overcome the problem in the 7-Var BDT, we perform the analysis with a new 2-step BDT method. In the first step, we use the 8 variables as in the standard BDT to discriminate between the VBF and the SM backgrounds including  $t\bar{t}$  and  $WW$ . Whereas in the second step, we focus on discriminating the VBF and ggF using the most powerful discriminators as those used in 7-Var BDT. Figure 7 shows the 2-step BDT output distributions after both steps. The left panel shows the normalized distribution of  $O_{\text{BDT}}^1$ , in which near the  $-1$  end is more background-like and near the  $+1$  end is more signal-like. Similarly, the right panel shows the normalized distribution of  $O_{\text{BDT}}^2$  after applying a cut of  $O_{\text{BDT}}^1 > 0.9$ . In a moment, we shall show that the cut value on  $O_{\text{BDT}}^1 > 0.9$  is the optimal choice with respect to the VBF purity and ggF contamination.

Figure 8 shows the VBF purity and ggF contamination versus the cut values of  $O_{\text{BDT}}^1$  (each event has a larger value than the cut value). It is important to note that the choices of  $O_{\text{BDT}}^1$  and  $O_{\text{BDT}}^2$  cut values are determined with the signal efficiency fixed (the signal event number is fixed at 5.1 events for various BDT methods). For example, if  $O_{\text{BDT}}^1$  cut is set at 0.9 (0.5), then  $O_{\text{BDT}}^2$  cut at 0.166 (0.425), such that the VBF event number is fixed at 5.1. Therefore, in Fig. 8 each  $O_{\text{BDT}}^1$  cut value corresponds to a  $O_{\text{BDT}}^2$  cut such that the signal event number is fixed at 5.1. It is clear and evident that we shall have purer VBF signal sample when we impose a more stringent cut. Also, the ggF contamination increases slightly as the cut gets more severe. The first-step-BDT output cut value is optimized at 0.9 to obtain the highest purity of VBF and the lowest ggF contamination. As shown in Table VI, with this new method of 2-step BDT we can

BDT method	Event number				VBF purity of	ggF
	VBF	ggF	$t\bar{t}$	$WW$	all processes	contamination
Standard BDT	5.13	0.73	0.40	0.45	76.42%	12.38%
11-Var BDT	5.11	0.61	0.32	0.43	79.05%	10.66%
7-Var BDT	5.11	0.55	2.89	1.58	50.49%	9.70%
2-step BDT ( $O_{\text{bdt}}^1 > 0.9$ )	5.10	0.44	0.51	0.56	77.09%	7.93%

TABLE VI. Summary of the results for the event numbers of each process, VBF purity, and ggF contamination in  $WW$  decay channel, after applying cuts on various methods of BDT. Here the ggF contamination is defined as  $N(\text{ggF}) / (N(\text{ggF}) + N(\text{VBF}))$ . The event numbers are normalized to  $5.8 \text{ fb}^{-1}$ . The luminosity here is taken to be the same as in Ref. [6] for direct comparison.

highly reduce the ggF contamination down from 12.38 to 7.93%, and at the same time maintain the VBF purity of 77%.

## B. $H \rightarrow \gamma\gamma$

In Fig. 9, we show the linear correlations between any two variables that we have used in the channel  $H \rightarrow \gamma\gamma$  analyses. We can see that strong correlations among the 3 jet-shape variables, and between  $\Delta\eta_{jj}$  and  $m_{jj}$  in both the signal and background samples. In addition, in order to avoid overtraining in the BDT analyses, we show the BDT output distributions for both the training and testing samples as shown in Fig. 10.

The results of our analyses in the channel  $H \rightarrow \gamma\gamma$  are summarized in Table VII. We control the VBF efficiency at 5.4% for comparison. The 9-Var BDT, which adds 3 new jet-shape variables compared to the standard BDT, can enhance the VBF purity and at the same time reduce the ggF contamination by about 2%. In order to focus on distinguishing between the VBF and ggF event samples, the 5-Var BDT, which uses the most powerful 5 variables, is introduced and can further decrease the ggF contamination by about 2%. However, this method sacrifices the discrimination from the other SM backgrounds and lowers the VBF purity to only 24.6%.

Similar to the previous channel, we attempt the 2-step BDT method to this case. We use the standard 6 variables in the first step to discriminate between the VBF and  $\gamma\gamma + jj$  background. In the second step, we separate between the VBF and ggF using the most powerful 5 discriminators as

BDT method	VBF efficiency	Event number			VBF purity of all processes	ggF contamination
		VBF	ggF	$\gamma\gamma + jj$		
Standard BDT	5.4%	6.19	1.44	10.41	34.3%	18.89%
9-Var BDT	5.4%	6.20	1.28	9.59	36.3%	17.08%
5-Var BDT	5.4%	6.19	1.12	17.86	24.6%	15.33%
2-step BDT ( $O_{\text{bdt}}^1 > 0.75$ )	5.4%	6.19	0.97	13.32	30.2%	13.59%

TABLE VII. Summary of the results for the event numbers of each process, VBF purity, ggF contamination in diphoton decay channel, after applying cuts on various methods of BDT. The event numbers are normalized to  $13.3 \text{ fb}^{-1}$ . The luminosity here is taken to be the same as in Ref. [7] for direct comparison.

those used in 5-Var BDT. Figure 11 shows the 2-step BDT output distribution in both steps. The left panel shows the normalized distribution of  $O_{\text{BDT}}^1$  while the right panel shows the normalized distribution of  $O_{\text{BDT}}^2$  after applying a cut of  $O_{\text{BDT}}^1 > 0.75$ . Figure 12 shows the VBF purity and ggF contamination versus the cut value of  $O_{\text{BDT}}^1$ . Similar to the previous channel, the choices of  $O_{\text{BDT}}^1$  and  $O_{\text{BDT}}^2$  cut values are determined with the signal efficiency fixed at 5.4% for various BDT methods. Therefore, each  $O_{\text{BDT}}^1$  cut value in Fig. 12 corresponds to a  $O_{\text{BDT}}^2$  cut such that the VBF signal efficiency is fixed at 5.4%. Again, we can achieve a purer VBF signal sample but with a slightly larger ggF contamination when we apply a more stringent cut value. The cut value of  $O_{\text{BDT}}^1$  is optimized at 0.75 for the highest purity of VBF and the lowest ggF contamination. As shown in Table VII, the ggF contamination is substantially reduced from 18.89% to 13.59%, and at the same time maintain the VBF purity at about 30.2%.<sup>4</sup>

### C. Receiver Operating Characteristic (ROC) curves

Statistically, it is useful to present the effectiveness of various methods using the ROC curves, so that one can easily read the effectiveness of various BDT off the ROC curves. Here we show parametrically the ggF rejection rate ( $y$ -axis) versus the VBF efficiency ( $x$ -axis). On one side it is the VBF efficiency that we prefer to be large while on the other side is the ggF rejection rate that

<sup>4</sup> The ggF contamination that we obtained by the standard BDT in the channel  $H \rightarrow \gamma\gamma$  is somewhat smaller (about 6%) than that obtained in ATLAS [7]. We presume the discrepancy is due to the uncertainty in detector simulations as we use DELPHES while ATLAS uses GEANT4.

we want to be as close to 100% as possible. However, in reality the higher VBF efficiency the lower the ggF rejection will be. We show the ROC curves for the  $H \rightarrow WW$  and  $H \rightarrow \gamma\gamma$  channels in Fig. 13 and Fig. 14, respectively, where we show the ggF rejection rate vs VBF efficiency. Note that in the 2-step BDT we have set  $O_{\text{BDT}}^1 > 0.9$  (0.75) for  $H \rightarrow WW$  ( $H \rightarrow \gamma\gamma$ ) channel before we vary  $O_{\text{BDT}}^2$  in the figures. In  $H \rightarrow WW$  channel, the 2-step BDT achieves the best ggF rejection, and thus the least ggF contamination. This is consistent with the ggF contamination shown in Table VI. Similarly, in  $H \rightarrow \gamma\gamma$  channel, the 2-step BDT offers the best for ggF rejection.

## V. CONCLUSIONS

We have studied the performance of the approach of 2-step boosted decision trees. We have followed as closely as the way that the ATLAS generated the event samples of VBF, ggF, and the corresponding SM backgrounds in the channels of  $H \rightarrow WW^*$  and  $H \rightarrow \gamma\gamma$ . In the first step, we trained the VBF signal against the SM backgrounds without the ggF sample, while in the second step we trained the VBF signal against the ggF sample.

We have demonstrated with our new approach of 2-step BDT, we can achieve a significant reduction of the ggF contamination from 12% (19%) down to 8% (12%) for  $H \rightarrow WW^*$  ( $H \rightarrow \gamma\gamma$ ). At the same time, we can maintain or slightly improve the overall purity of the VBF sample among all the backgrounds.

The approach of this study can be applied to other decay channels, such as  $H \rightarrow ZZ^*$ ,  $\tau\tau$ , and  $b\bar{b}$ . Further investigations can include optimization of the number of variables used in each step in the 2-step BDT. Actually, one can use various ways to rank the importance of each variable.

## ACKNOWLEDGMENTS

This research was supported in parts by the MoST of Taiwan under Grant Nos. MOST-105-2112-M-007-028-MY3 and MOST-103-2112-M-007-024-MY3.

- 
- [1] G. Aad *et al.* [ATLAS Collaboration], Phys. Lett. B **716**, 1 (2012) [arXiv:1207.7214 [hep-ex]]; S. Chatrchyan *et al.* [CMS Collaboration], Phys. Lett. B **716**, 30 (2012) [arXiv:1207.7235]

- [hep-ex]].
- [2] V. D. Barger, K. m. Cheung, T. Han, J. Ohnemus and D. Zeppenfeld, Phys. Rev. D **44**, 1426 (1991). doi:10.1103/PhysRevD.44.1426
  - [3] V. D. Barger, K. m. Cheung, T. Han and D. Zeppenfeld, Phys. Rev. D **44**, 2701 (1991) Erratum: [Phys. Rev. D **48**, 5444 (1993)]. doi:10.1103/PhysRevD.48.5444, 10.1103/PhysRevD.44.2701
  - [4] N. Kauer, T. Plehn, D. L. Rainwater and D. Zeppenfeld, Phys. Lett. B **503**, 113 (2001) doi:10.1016/S0370-2693(01)00211-8 [hep-ph/0012351].
  - [5] C. Anastasiou, C. Duhr, F. Dulat, E. Furlan, T. Gehrmann, F. Herzog, A. Lazopoulos and B. Mistlberger, JHEP **1605**, 058 (2016) doi:10.1007/JHEP05(2016)058 [arXiv:1602.00695 [hep-ph]];  
C. Anastasiou, C. Duhr, F. Dulat, F. Herzog and B. Mistlberger, Phys. Rev. Lett. **114**, 212001 (2015) doi:10.1103/PhysRevLett.114.212001 [arXiv:1503.06056 [hep-ph]].
  - [6] The ATLAS collaboration [ATLAS Collaboration], ATLAS-CONF-2016-112;  
G. Aad *et al.* [ATLAS Collaboration], Phys. Rev. D **92**, no. 1, 012006 (2015) doi:10.1103/PhysRevD.92.012006 [arXiv:1412.2641 [hep-ex]].
  - [7] The ATLAS collaboration [ATLAS Collaboration], ATLAS-CONF-2016-067;  
G. Aad *et al.* [ATLAS Collaboration], Phys. Rev. D **90**, no. 11, 112015 (2014) doi:10.1103/PhysRevD.90.112015 [arXiv:1408.7084 [hep-ex]].
  - [8] S. Alioli, P. Nason, C. Oleari and E. Re, JHEP **1006**, 043 (2010) doi:10.1007/JHEP06(2010)043 [arXiv:1002.2581 [hep-ph]].
  - [9] P. Nason and C. Oleari, JHEP **1002**, 037 (2010) doi:10.1007/JHEP02(2010)037 [arXiv:0911.5299 [hep-ph]].
  - [10] S. Alioli, P. Nason, C. Oleari and E. Re, JHEP **0904**, 002 (2009) doi:10.1088/1126-6708/2009/04/002 [arXiv:0812.0578 [hep-ph]].
  - [11] H. L. Lai, M. Guzzi, J. Huston, Z. Li, P. M. Nadolsky, J. Pumplin and C.-P. Yuan, Phys. Rev. D **82**, 074024 (2010) doi:10.1103/PhysRevD.82.074024 [arXiv:1007.2241 [hep-ph]].
  - [12] T. Sjostrand, S. Mrenna and P. Z. Skands, Comput. Phys. Commun. **178** (2008) 852 doi:10.1016/j.cpc.2008.01.036 [arXiv:0710.3820 [hep-ph]].
  - [13] J. de Favereau *et al.* [DELPHES 3 Collaboration], JHEP **1402**, 057 (2014) [arXiv:1307.6346 [hep-ex]].

- [14] J. Alwall *et al.*, JHEP **1407**, 079 (2014) doi:10.1007/JHEP07(2014)079 [arXiv:1405.0301 [hep-ph]].
- [15] T. Melia, P. Nason, R. Rontsch and G. Zanderighi, JHEP **1111**, 078 (2011) doi:10.1007/JHEP11(2011)078 [arXiv:1107.5051 [hep-ph]].
- [16] T. Sjostrand, S. Mrenna and P. Z. Skands, JHEP **0605**, 026 (2006) doi:10.1088/1126-6708/2006/05/026 [hep-ph/0603175].
- [17] A. Hocker *et al.*, “TMVA - Toolkit for Multivariate Data Analysis,” PoS ACAT , 040 (2007) [physics/0703039 [PHYSICS]].
- [18] J. Shelton, doi:10.1142/9789814525220\_0007 arXiv:1302.0260 [hep-ph].



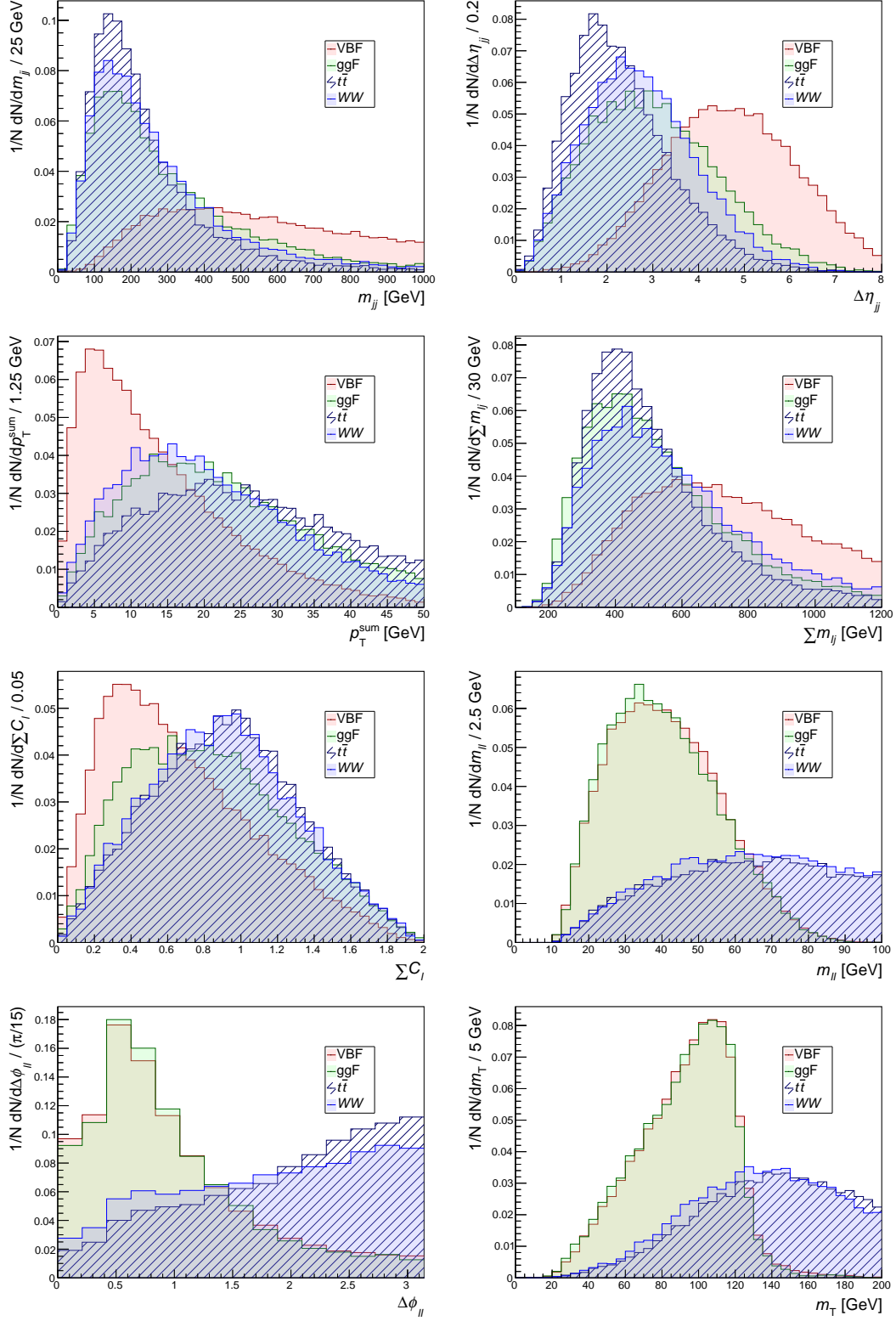


FIG. 1. Distributions of various variables used in the standard BDT in the  $H \rightarrow WW^*$  channel for the VBF signal, ggF, and the SM backgrounds.

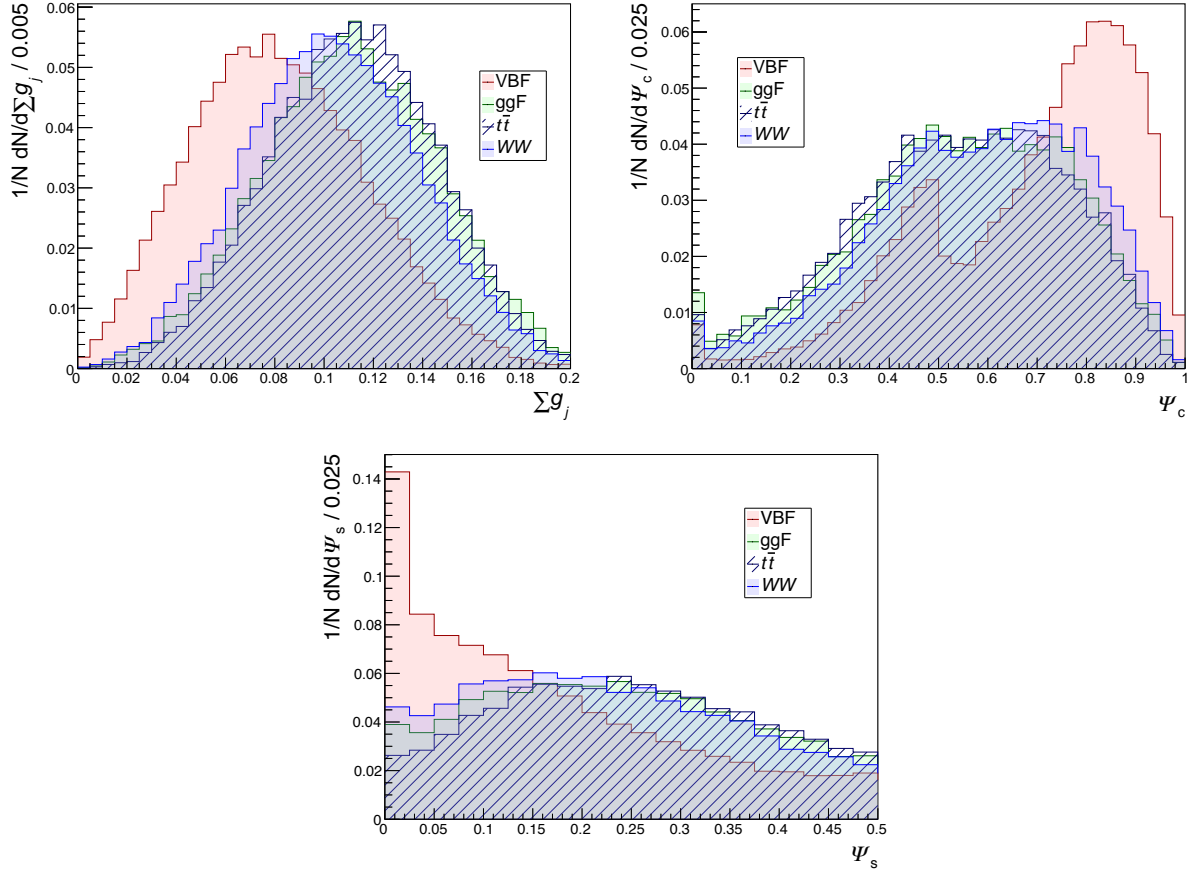


FIG. 2. Distributions of the 3 jet-shape variables used in the  $H \rightarrow WW^*$  channel.

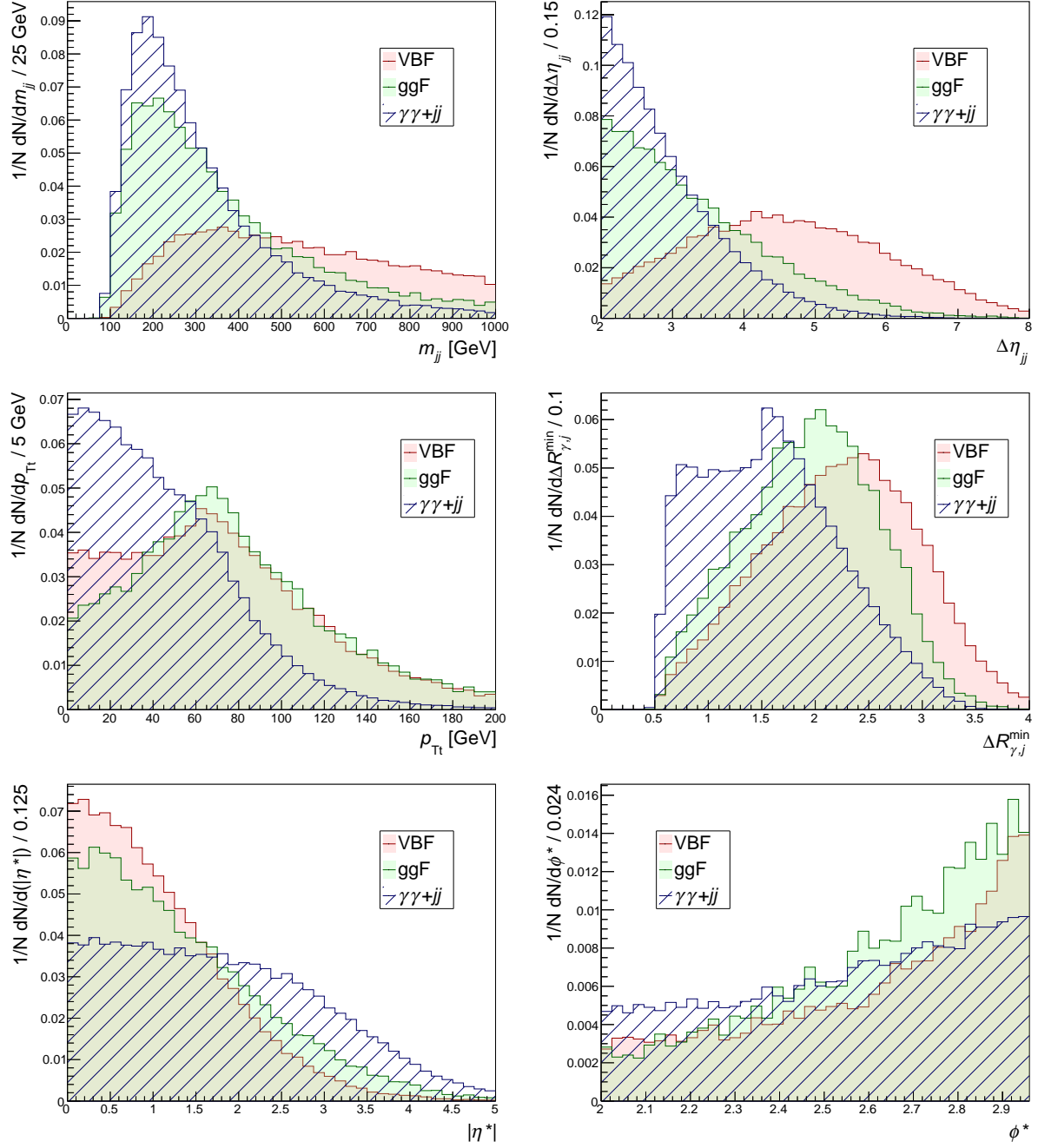
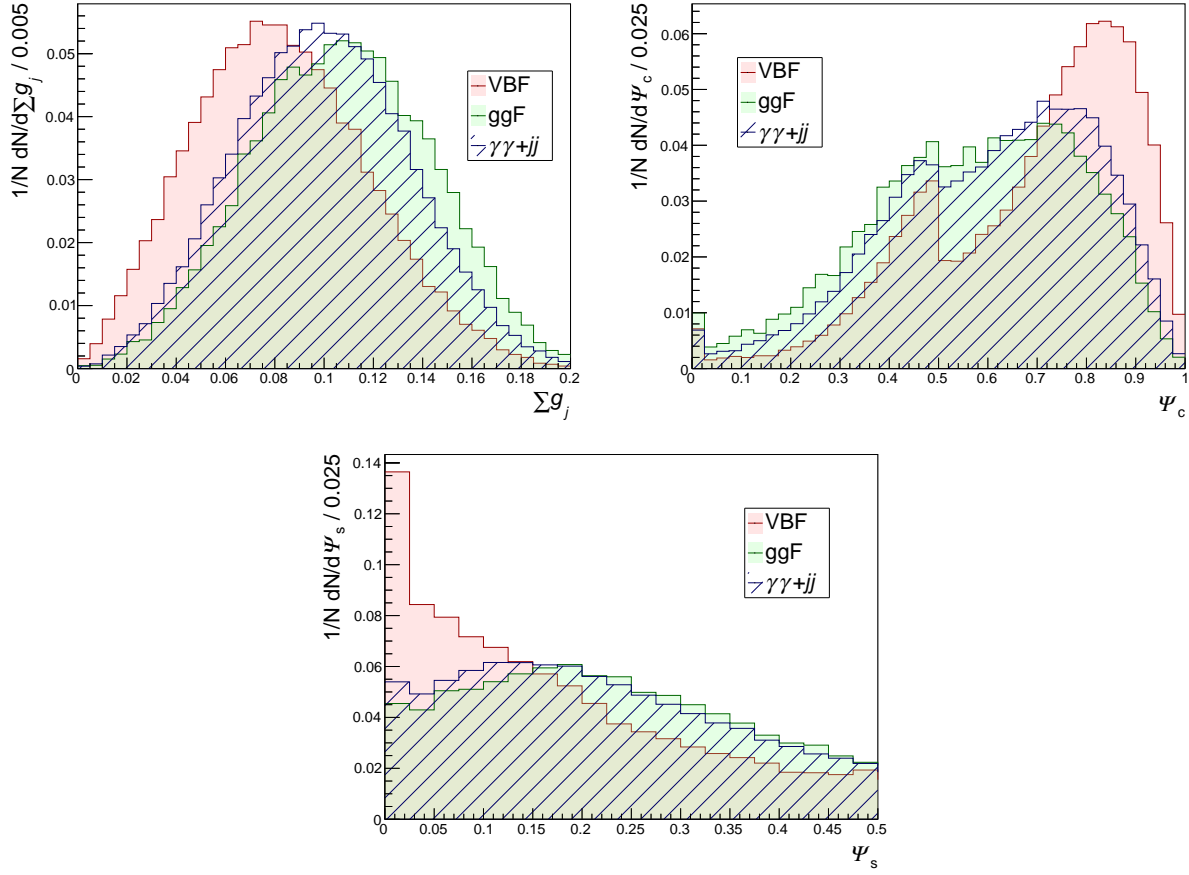
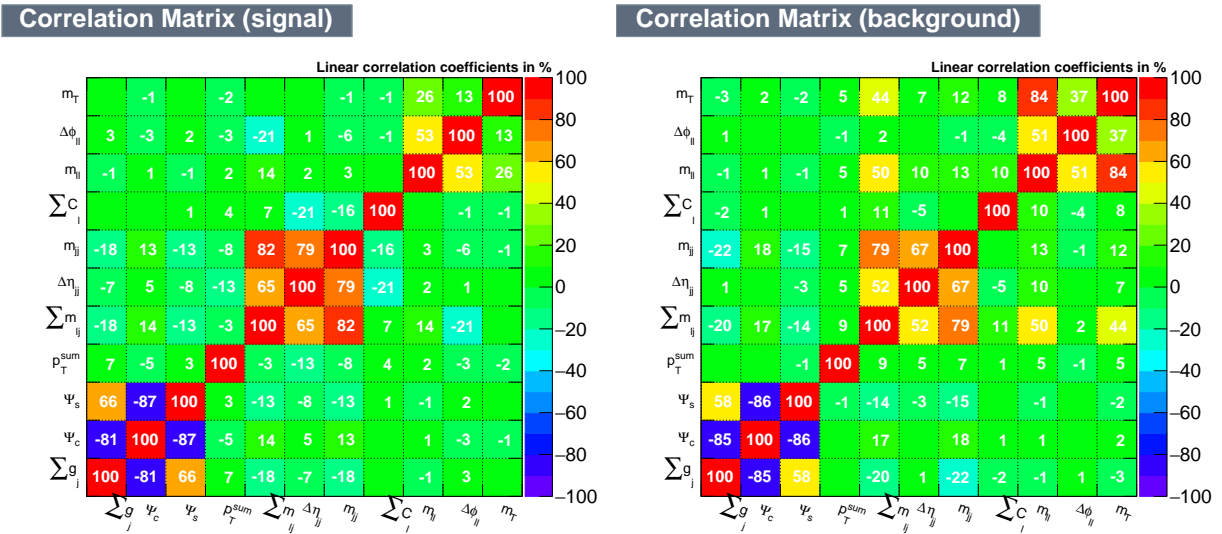


FIG. 3. Distributions of the 6 variables used in the channel  $H \rightarrow \gamma\gamma$  for the VBF signal, ggF, and the SM background  $\gamma\gamma jj$ .

FIG. 4. Distributions of the 3 jet-shape variables used in the channel  $H \rightarrow \gamma\gamma$ .FIG. 5. Linear correlations between any two variables in the channel  $H \rightarrow WW^* \rightarrow e\nu\mu\nu$  used in the 11-Var BDT. The left panel shows the VBF while the right panel includes ggH,  $t\bar{t}$ , and WW.

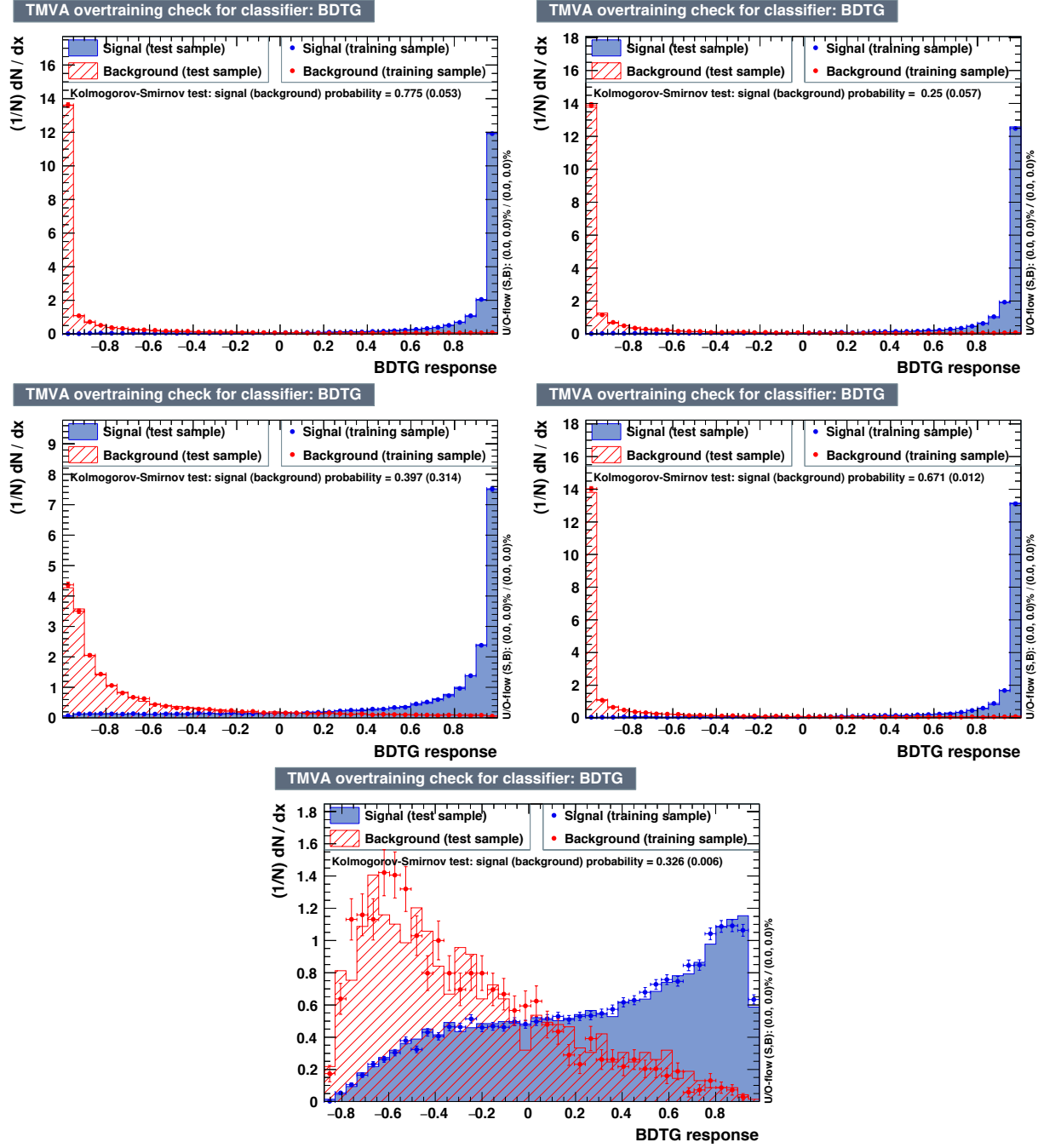


FIG. 6. BDT output distributions of training and test samples in  $H \rightarrow WW^*$ . (*Top-left*) Method of standard BDT. (*Top-right*) Method of 11-Var BDT. (*Middle-left*) Method of 7-Var BDT. (*Middle-right*) The first step in the 2-step BDT. (*Bottom*) The second step in the 2-step BDT. Note that half of sample is used as the training sample and the other half as the testing sample.

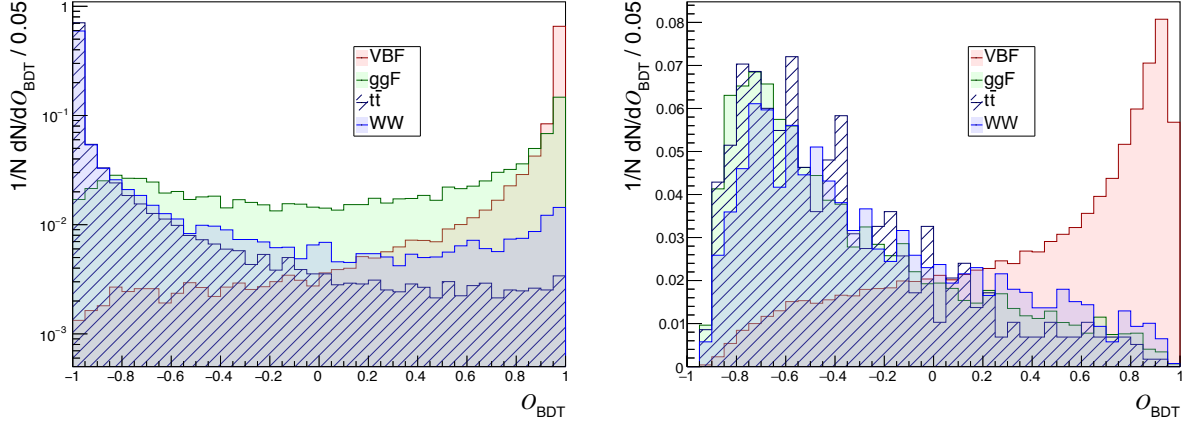


FIG. 7. 2-step BDT output distributions in first step(left) and second step(right) for each process in  $H \rightarrow WW^*$ .

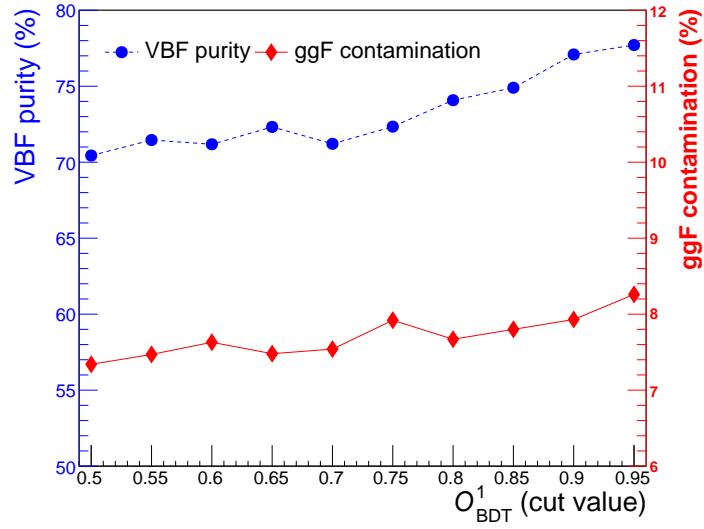


FIG. 8. Combined plot of VBF purity and ggF contamination in  $H \rightarrow WW^*$  versus the cut value on  $O_{\text{BDT}}^1$ .

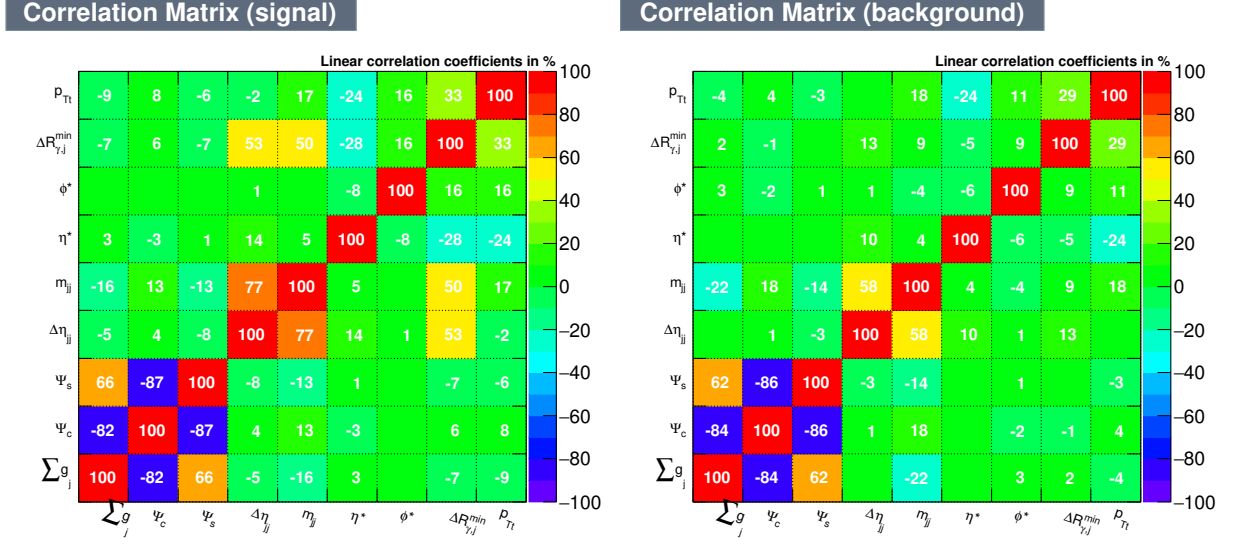


FIG. 9. Linear correlation of each variable used in BDT in  $H \rightarrow \gamma\gamma$ . In this figure, the signal (left) denotes VBF, and the background (right) includes ggH as well as  $\gamma\gamma + jj$ .

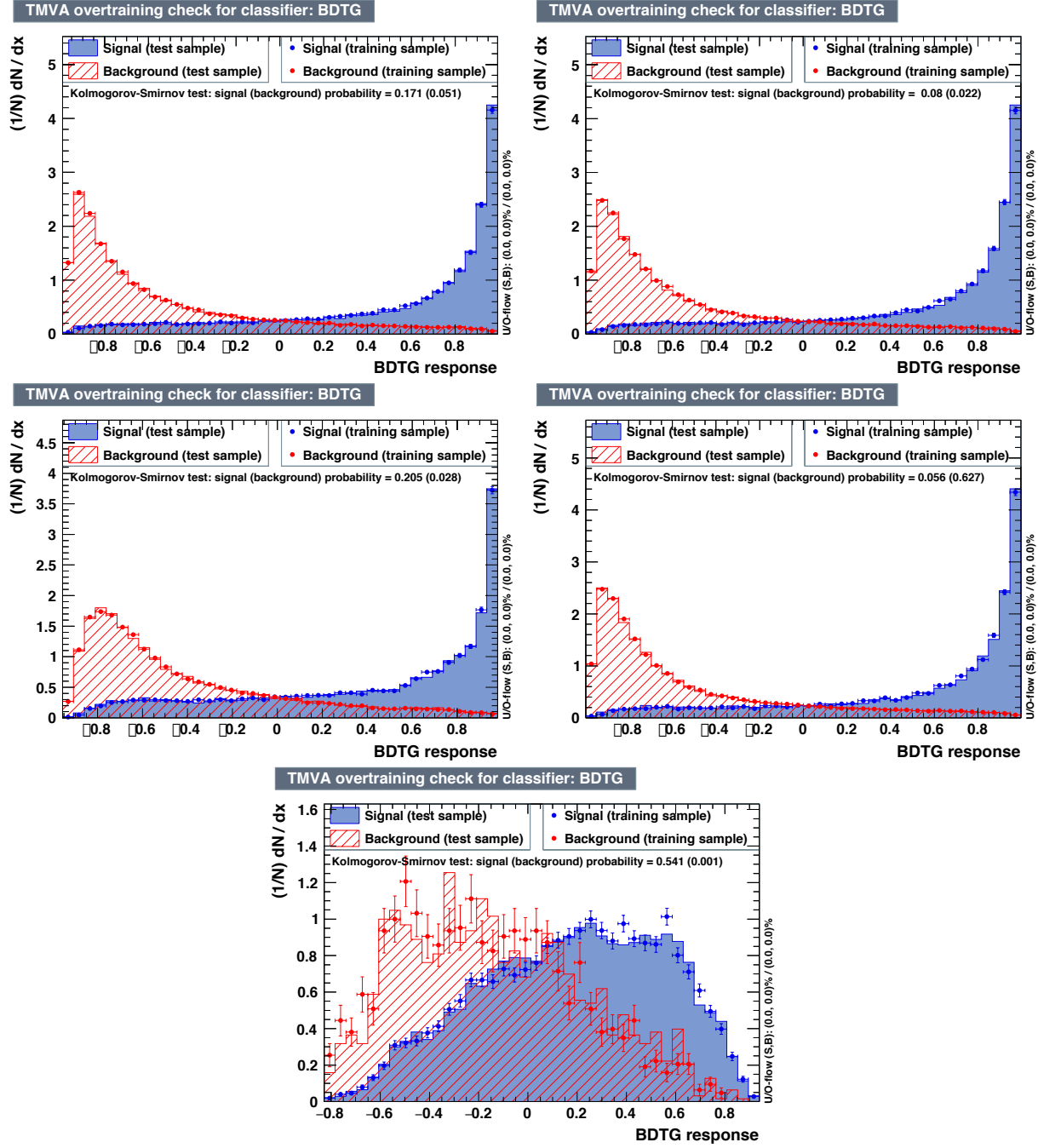


FIG. 10. BDT output distribution of training and testing samples in  $H \rightarrow \gamma\gamma$ . (*Top-left*) Method of standard BDT. (*Top-right*) Method of 9-Var BDT. (*Middle-left*) Method of 5-Var BDT. (*Middle-right*) The first step in the 2-step BDT. (*Bottom*) The second step in the 2-step BDT. Note that half of sample is used as the training sample and the other half as the testing sample.



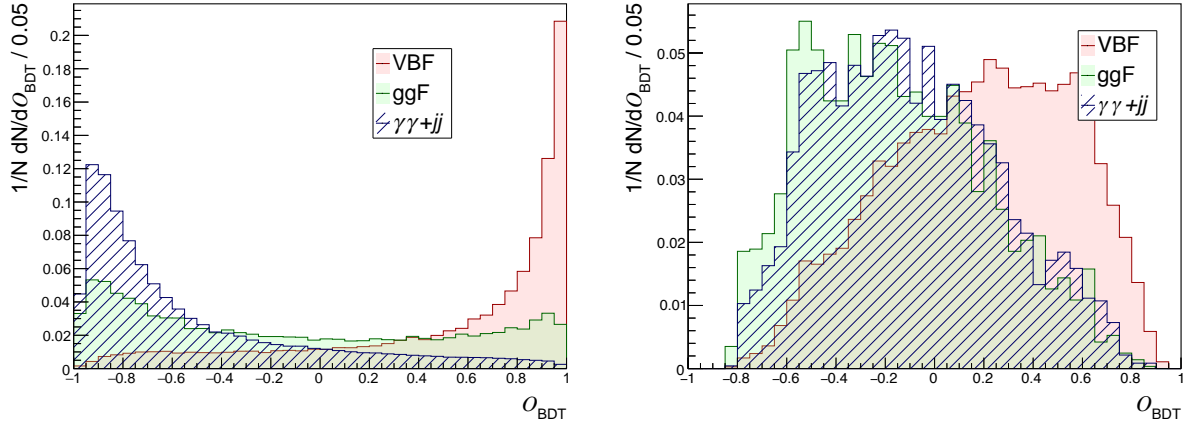


FIG. 11. 2-step BDT output distributions in first step (left) and second step (right) for each process in  $H \rightarrow \gamma\gamma$ .

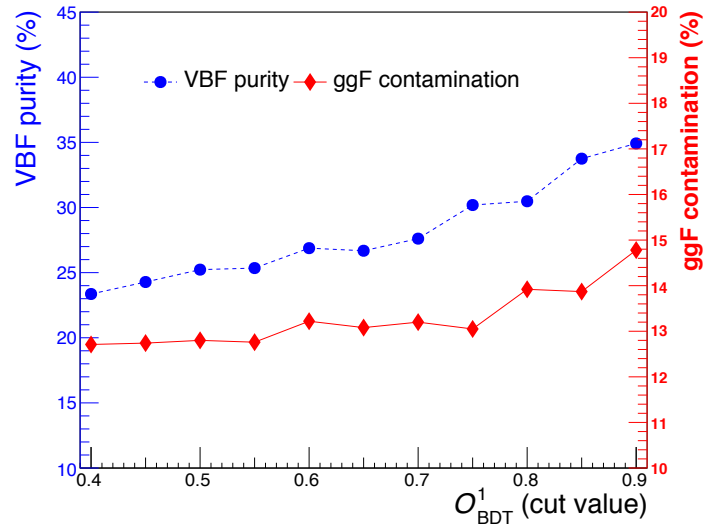


FIG. 12. Combined plot of VBF purity and ggF contamination in  $H \rightarrow \gamma\gamma$  versus the cut value on  $O_{\text{BDT}}^1$ .

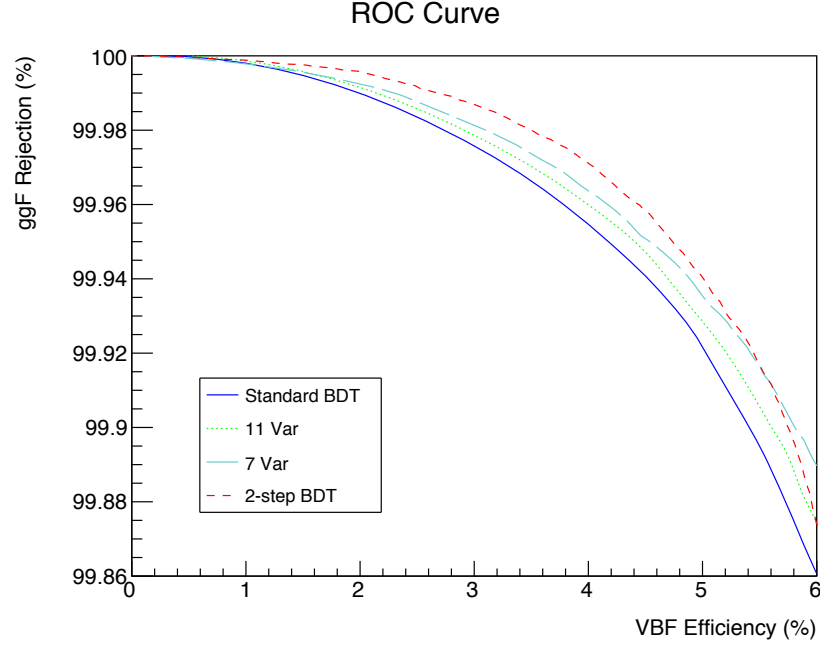


FIG. 13. The ROC curves for ggF rejection vs VBF efficiency for various BDT methods used in  $H \rightarrow WW^*$  channel. For the 2-step BDT we have imposed  $O_{\text{BDT}}^1 > 0.9$  and then vary  $O_{\text{BDT}}^2$ . As indicated in Table VI the final VBF efficiency is set at 3.8% where the event numbers for VBF and ggF in the 2-step BDT are 5.10 and 0.44, respectively.

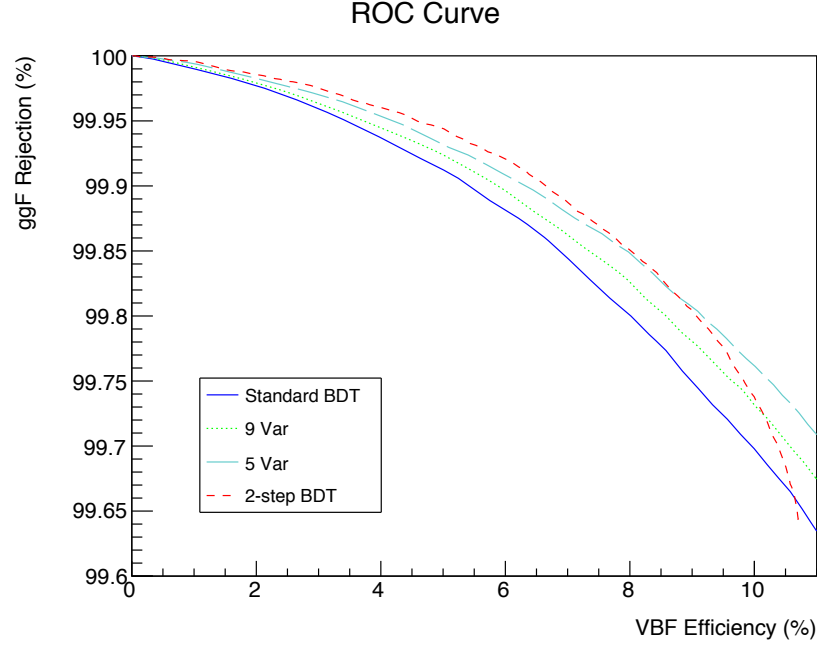


FIG. 14. The ROC curves for ggF rejection vs VBF efficiency for various BDT methods used in  $H \rightarrow \gamma\gamma$  channel. For the 2-step BDT we have imposed  $O_{\text{BDT}}^1 > 0.75$  and then vary  $O_{\text{BDT}}^2$ . As indicated in Table VII the final VBF efficiency is set at 5.4% where the event numbers for VBF and ggF in the 2-step BDT are 6.19 and 0.97, respectively.